Air Stable p-Doping of WSe_2 by Covalent Functionalization

Peida Zhao,[†,‡] Daisuke Kiriya,[†,‡] Angelica Azcatl,[§] Chenxi Zhang,[§] Mahmut Tosun,[†,‡] Yi-Sheng Liu,[∥] Mark Hettick,[†,‡] Jeong Seuk Kang,[†,‡] Stephen McDonnell,[§] Santosh KC,[§] Jinghua Guo,[∥] Kyeongjae Cho,[§] Robert M. Wallace,[§] and Ali Javey*[,†,‡]

[†]Electrical Engineering and Computer Sciences, University of California, Berkeley, California 94720, United States, [‡]Materials Sciences Division, Lawrence Berkeley National Laboratory, Berkeley, California 94720, United States, [§]Materials Science and Engineering, The University of Texas at Dallas, Richardson, Texas 95080, United States, and [∥]Advanced Light Source, Lawrence Berkeley National Laboratory, Berkeley, California 94720, United States

ABSTRACT Covalent functionalization of transition metal dichalcogenides (TMDCs) is investigated for air-stable chemical doping. Specifically, p-doping of WSe_2 *via* NO_x chemisorption at 150 °C is explored, with the hole concentration tuned by reaction time. Synchrotron based soft X-ray absorption spectroscopy (XAS) and X-ray photoelectron spectroscopy (XPS) depict the formation of various $WSe_{2-x-y}O_xN_y$ species both on the surface and interface between layers upon chemisorption reaction. *Ab initio* simulations corroborate our spectroscopy results in identifying the energetically favorable complexes, and predicting WSe_2:NO at the Se vacancy sites as the predominant dopant species. A maximum hole concentration of $\sim 10^{19}$ cm^{-3} is obtained from XPS and electrical measurements, which is found to be independent of WSe_2 thickness. This degenerate doping level facilitates 5 orders of magnitude reduction in contact resistance between Pd, a common p-type contact metal, and WSe_2. More generally, the work presents a platform for manipulating the electrical properties and band structure of TMDCs using covalent functionalization.

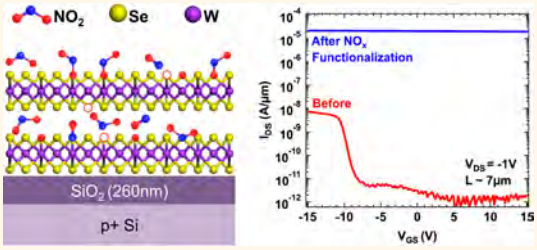

KEYWORDS: layered materials · covalent binding · NO_2 · chemisorption · doping

Transition metal dichalcogenides (TMDCs) have garnered much attention in the recent years due to their unique material properties and potential applications in various electronic and optical devices.[1,2] Possessing a layered structure with a monolayer thickness of down to 7 Å, TMDCs represent a viable electronic material system for future devices, especially as size scaling continues to the sub-10 nm regime. To facilitate TMDC integration into future electronic devices, doping becomes a vital stepping-stone. Indeed, many exploratory works have already reported both n- and p-doping utilizing surface charge transfer mechanisms aided by molecular physisorption.[3−5] For instance, WSe_2 has been p-doped using physisorbed NO_2; while this doping scheme has achieved superb p-type field-effect transistors (FETs), the doping is unstable and decays almost completely within an hour.[4] The instability is due to the physisorption process, which relies on weak van der Waals (vdW) interactions incapable of sustaining stable electron transfers at ambient conditions. Moving forward, an *air stable* doping scheme is needed as a fundamental enabler toward the integration of TMDCs into robust device fabrications.

In this work, we demonstrate air stable p-doping, up to the degenerate limit, by *chemisorption* of NO_2 on WSe_2 performed at a sample temperature of 150 °C. Synchrotron-based soft X-ray absorption spectroscopy (XAS) and X-ray photoelectron spectroscopy (XPS) depict formation of various $WSe_{2-x-y}O_xN_y$ species upon NO_x chemisorption on WSe_2. Formation of these species and their effects on the electronic properties of WSe_2 are also examined by *ab initio* simulations, which confirm the experimental observations. Notably, the chemisorption process retains WSe_2's long-range crystal structure and optical properties. This doping process leads to a 5 orders of magnitude reduction in contact resistance (R_c) between WSe_2 and Pd metal, and results in a degenerate doping concentration of 1.6×10^{19} cm^{-3}. From this study, we exhibit a

* Address correspondence to ajavey@berkeley.edu.

Received for review August 16, 2014 and accepted September 17, 2014.

Published online September 17, 2014
10.1021/nn5047844

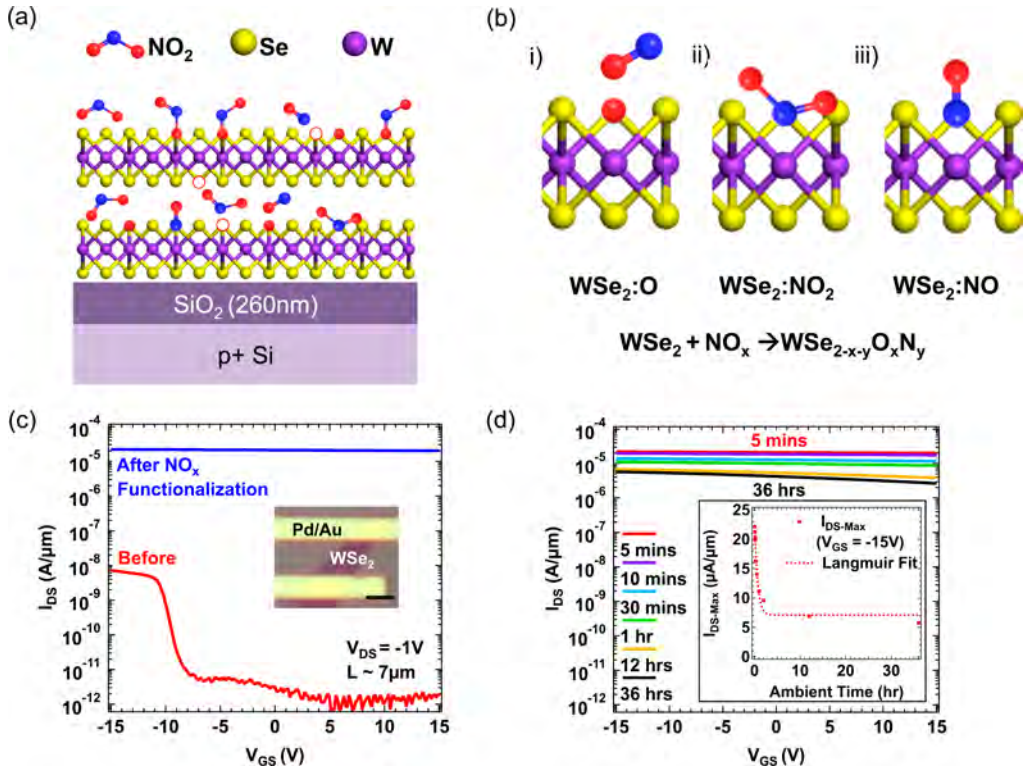

Figure 1. (a) Schematic of NO_x chemisorption process at the WSe_2 bulk and surface. (b) Proposed specific NO_x chemisorption at the selenium vacancy sites can lead to three distinct configurations: (i) WSe_2:O, (ii) WSe_2:NO_2, (iii) WSe_2:NO. (c) $I_{DS}-V_{GS}$ of before and after NO_2 treated devices. Inset: Optical microscopy of fabricated device using Pd/Au contacts; scale bar is 2 μm. (d) Initial current drop after doping is attributed to desorption of weakly physisorbed NO_2. Inset: Drain current change is fitted to a time-dependent Langmuir isotherm desorption model *vs* air exposure time. Dash line represents fitted curve.

route toward an air stable p-doping method on WSe_2 that can be efficiently utilized for various device schemes in the future.

RESULTS AND DISCUSSION

A back-gated WSe_2 FET is fabricated *via* standard electron beam lithography or photolithography and exposed to NO_2 at 150 °C for a set reaction time of 4−12 h. Given the strong oxidizing nature of NO_2, we predict an induced NO_x chemisorption process on WSe_2 due to the temperature and treatment time utilized. A defect-oriented model is proposed where NO_2 chemisorbs on WSe_2 surface and bulk defect sites (*e.g.*, selenium vacancies), forming stable electron withdrawing $WSe_{2-x-y}O_xN_y$ species that lead to p-doping (Figure 1a,b). At the temperatures used here, NO_2 gas is partly decomposed to form O and NO,[6,7] making various covalent functionalization schemes possible. Figure 1b depicts three most likely scenarios. Figure 1b (i) shows direct W oxidation resulting from the O of NO_2 occupying a Se vacancy followed by NO_2 thermal disassociation and desorption of NO. Figure 1b (ii) shows the alternative NO_2 adsorption configuration with N directly bonding to W at the presence of a Se vacancy. Figure 1b (iii) illustrates N of NO covalently bonded with W, where NO is created through NO_2 disassociation.

Transfer characteristics of doped devices are measured before and after NO_x functionalization (Figure 1c). Here the thickness of WSe_2 flake is ∼5 nm. Before NO_2 exposure, we observe a clear p-FET characteristic with an on/off ratio of ∼1000 and a low I_{on} of $\sim 10^{-8}$ A/μm due to severe contact resistance resulting from the Schottky barrier present between WSe_2 and Pd.[4] After NO_x chemisorption, we observe a drastic increase of I_{on} by about 1000×, and gate's inability to control the channel conduction. Gate control loss is due to hole doping by NO_x chemisorption that moves the Fermi level (E_F) to close proximity of the valence band edge (E_V). The excessive states present in the vicinity of E_F then render gate modulation of E_F ineffective, reflecting a degenerate p-doping situation. The doping stability is studied by examining the changing transfer characteristics of the doped sample upon air exposure. As seen in Figures 1d and Supporting Information Figure S1, the device undergoes a gradual current drop for the first 2−3 h, and eventually stabilizes at a set current level. This initial current drop is attributed to desorption of physisorbed NO_x species leaving the WSe_2. As expected, our doping mechanism is a combination of NO_x physi- and chemisorption on WSe_2 where *only* chemisorbed NO_x contributes to stable doping. The falling current *versus* time is fit to Langmuir isotherm assuming current being directly related to the physisorbed NO_x *via*

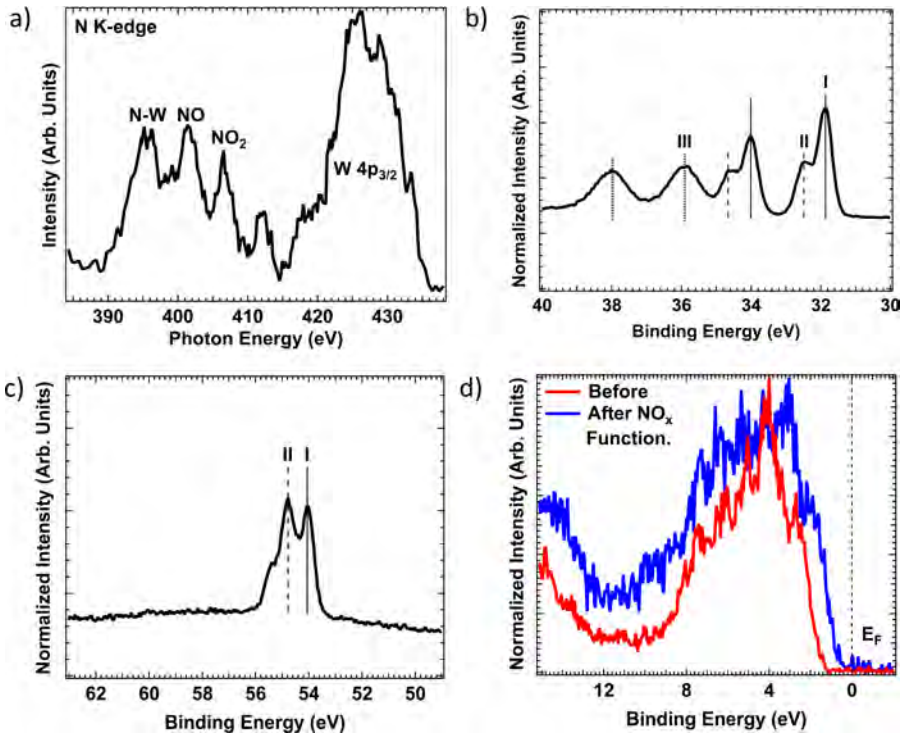

Figure 2. (a) Total electron yield of Soft X-ray Absorption Spectroscopy (XAS) NO_2 doped samples. Identifiable peaks N K-edge indicates N−W, NO, and NO_2 species in host after NO_x chemisorption. (b) Tungsten core level *via* X-ray Photoelectron Spectroscopy (XPS) showing the formation of various $WSe_{2-x-y}O_xN_y$ species. Labels I, II, and III indicate W doublets of different oxidation states. (c) Se 3d core level after NO_x chemisorption. Labels I and II indicate two different species of different Se oxidation states. (d) Valence band edge of WSe_2 before and after NO_x; a definitive ~0.8 eV shift of the valence band edge is shown with respect to the Fermi level.

$I(t) = \{I_{initial} + [\psi/(1+\psi)][1 - e^{-(t/\tau)}]\}$ where t is the air exposure time, $I_{initial}$ is the initial current level right after chemisorption, ψ is a dimensionless parameter characterizing surface coverage, and τ is the desorption time constant. We extract the desorption time constant $\tau \sim 40$ min from NO_x physisorption, comparable to other physisorption-based gas sensors (such as ion-sensitive FET sensors) operating at room temperature.[8] Notably, the doping effect is irreversible even after thermal annealing of the sample at 300 °C in Ar, which further supports our proposed scheme of NO_x chemisorption leading to stable doping.

Given the stability of chemisorption, in-depth material characterization techniques in ultra-high vacuum (UHV) environments can be used to investigate the nature of chemisorbed species, in contrast with that of the unstable surface physisorbed molecules.[4,5] First, the nitrogen K absorption edge was examined using XAS. A collection of both total electron yield (penetration depth of ~10 nm) and total fluorescence yield (penetration depth of ~100 nm) show similar emission trend, signifying various nitrogen containing species in both depth regimes. The results suggest that the chemisorption is occurring at both the surface and interface between the layers of WSe_2. As a function of absorbed photon energy for N 1s electrons, a larger energy translates to a higher N oxidation state, as it becomes harder to remove electrons due to stronger electrostatic interactions. We observe 3 peaks at ~396, ~401, and ~406 eV which we assign to N−W (from W-NO_x species), NO, and NO_2 species, respectively, based on literature values.[9−14] Therefore, XAS results substantiate all three predicted configurations shown in Figure 1b.

Core W levels were investigated *via* XPS. According to Figure 2b, six visible peaks were observed after doping compared to only two visible peaks before NO_x chemisorption. The six peaks correspond to three doublets (each doublet possessing a unique W $4f_{5/2}$ and W $4f_{7/2}$ peak value), each doublet indicating a different W containing species with W of different oxidation states. Doublet III at 35.81 eV is assigned to WO_x with at an almost 6^+ oxidation state.[15,16] Doublets I and II (31.8 and 32.5 eV for W $4f_{7/2}$ values, respectively) are assigned to different stoichiometric ratio of $WSe_{2-x-y}O_xN_y$ species (also observable at the Se 3d level in Figure 2c) and corresponds to W oxidation state between 0 and 4^+ (ref 17). Note that the N stoichiometric ratio y is less than 0.003, corresponding to an atomic concentration of 0.1% and falling below the XPS detection limit. XAS, with a higher sensitivity due to Synchrotron excitation source, however, clearly identifies the N present and underlines the importance of using both XAS and XPS to probe the complete composition of the chemisorbed species present on WSe_2.

The valence band edge of WSe_2 was also examined by XPS. We observe a 0.8 eV shift of E_F (Figure 2d) upon

NO_x chemisorption with $E_V - E_F \sim 50$ meV extracted *via* linear extrapolation of the valence band tail. This large E_F shift is indicative of p-doping of WSe_2 and suggests a degenerate doping level ($E_V - E_F < 3kT$) by NO_x functionalization. From $E_V - E_F$, we extract a hole concentration of $p \sim 1.3 \times 10^{19}$ cm^{-3} by using the Joyce Dixon approximation[18] using an effective density of states[19] of N_v at 2.54×10^{19} cm^{-3}.

Subsequently, *ab initio* simulation (see Methods for details) was used to examine the thermodynamic stability of $WSe_{2-x-y}O_xN_y$ species after NO_x functionalization and the changing band structure of WSe_2 as a result. From density functional theory (DFT) calculations, we observe energetically favorable adsorption of O, NO and NO_2 at Se vacancies (Table 1), which is consistent with the experimental observations. Notably, on the basis of DFT calculations, adsorption was found to be unfavorable without the presence of Se vacancies.

Out of all adsorbates, only NO adsorption is predicted to contribute to p-doping of WSe_2 based on DFT simulations. Figure 3 shows the relaxed configuration of chemisorbed NO with N bonding to W, similar to Figure 1b (iii) configuration. By examining the band structure, we find that NO:WSe_2 configuration creates two defect bands close to the valence band edge shown in Figure 3b. The red dash line, overlapping with one of the NO adsorption induced defect bands, represents E_F. The other two chemisorbed species have minimal effects on the carrier concentration of WSe_2 based on the DFT simulations (Figure 3c).

Next we examine the effects of NO_x functionalization on the crystal structure and luminescence properties of WSe_2. X-ray diffraction (XRD), Raman spectroscopy and photoluminescence (PL) were all performed on NO_x functionalized WSe_2 samples. XRD data in Figure 4a demonstrates that the overall WSe_2 crystal structure remains intact as the two Miller index peaks 002 and 103 are preserved with similar intensities and no visible θ shifts. Figure 4b demonstrates the retention of the primary phonon modes E_{2g} and A_{1g} at 249 and 251 cm^{-1}, respectively, for a trilayer WSe_2 before and after doping, consistent with the literature.[20,21] PL spectra in Figure 4c shows the two peaks (1.47 and 1.6 eV) of a trilayer WSe_2 unaffected by NO_x chemisorption.[22,23] From our XRD, Raman and PL characterizations, we conclude that doping functionalization does not compromise the unique properties of WSe_2 at the macroscopic level.

Electrical measurements of WSe_2 devices before and after NO_x chemisorption were performed. Two studies were conducted, the first being a time dependent doping study at varying thicknesses. Figure 5a shows a representative transfer characteristic of 7.5 nm thick WSe_2 back-gated device as a function of NO_x doping time. A progressively heavier p-doping can be observed, reflected by an increasing I_{on} and diminishing gate control. The increasing I_{on} displays a degree of doping tunability *via* doping time, with I_{on} eventually saturating to degenerate behavior. Doping concentration is explicitly extracted across three devices with different flake thicknesses of 0.7, 7.5, and 78 nm

TABLE 1. Binding Energies of Three Adsorbates (NO_2, NO, O) on Se Vacancies of WSe_2[a]

adsorbates on Se vacancies		
$\Delta E_{NO2:WSe2}$	$\Delta E_{NO:WSe2}$	$\Delta E_{O:WSe2}$
−1.0 eV	−2.8 eV	−4.8 eV

[a] The error for binding energy is within 0.1 eV.

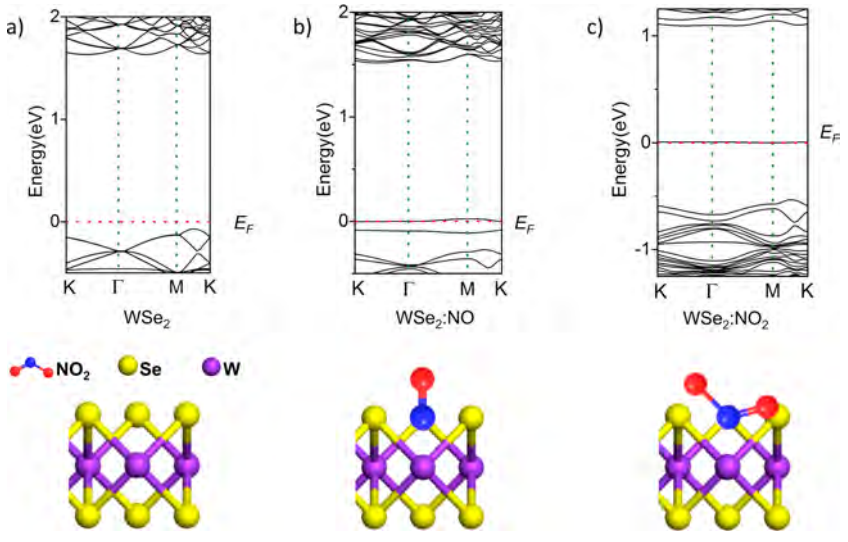

Figure 3. *Ab initio* simulation results showing band structure and corresponding simulated model of (a) pristine WSe_2, (b) WSe_2 with NO adsorption in Se vacancy, and (c) WSe_2 with NO_2 adsorption in Se vacancy. The red dotted line indicates the Fermi level.

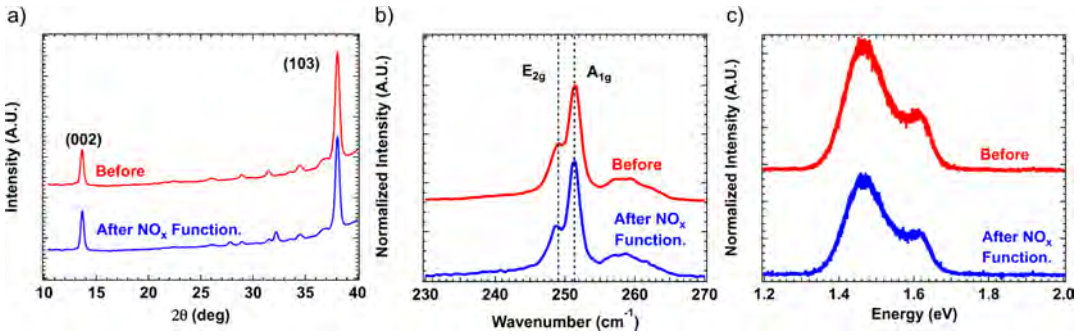

Figure 4. (a) X-ray diffraction (XRD) pattern of WSe_2 before and after WSe_2 functionalization. (b) Raman and (c) photoluminescence (PL) spectra of the same trilayer WSe_2 flake after NO_x chemisorption.

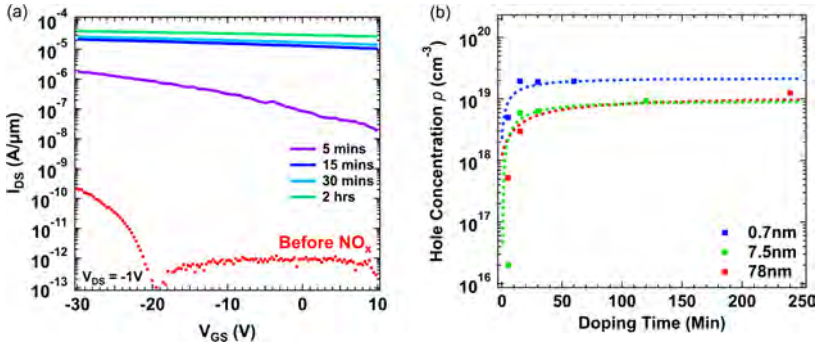

Figure 5. (a) Representative $I_{DS}-V_{GS}$ for WSe_2 device exposed to NO_2 at different functionalization time. (b) Extracted doping concentration *vs* doping time for different flake thicknesses. All doping levels saturate at $\sim 10^{19}$ cm^{-3}.

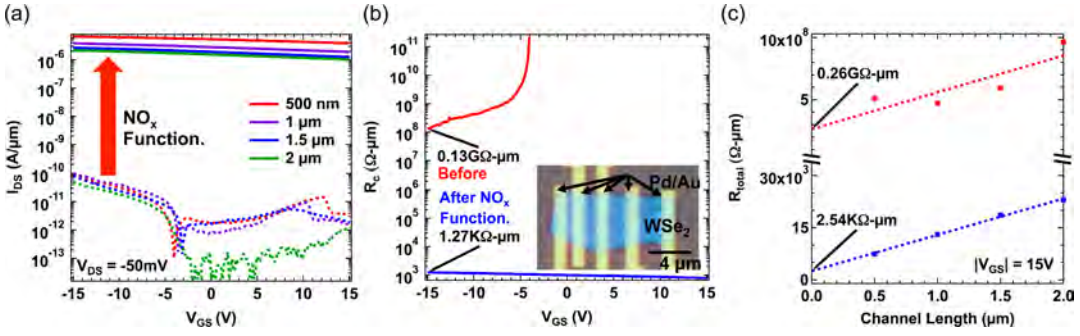

Figure 6. (a) $I_{DS}-V_{GS}$ of TLM device before and after NO_2 treatment, showing a (b) 5 orders of magnitude decrease in contact resistance. Inset: Optical microscopy of fabricated back-gated device used for TLM. (c) Extracted total resistance change before and after NO_x functionalization at $|V_{GS} = 15$ V|.

(monolayer thickness is determined by optical microscopy and the rest determined by AFM in Supporting Information Figure S2), respectively, *versus* doping time (Figure 5b). Assuming negligible R_c due to the thinning Schottky barrier at higher doping concentrations and therefore higher tunneling current, we can estimate doping concentration by first finding the 2D sheet charge density $n_{2D} = (I_{DS}L)/(qWV_{DS}\mu_p)$ at $V_G = 0$ where V_{DS} is the drain voltage, L and W are the length and width of the channel, q is the unit electron charge, and μ_p is the field effect hole mobility. From n_{2D}, we find volume doping concentration which saturates to $\sim 1 \times 10^{19}$ cm^{-3} across all three devices. The similar saturated doping level across all three devices demonstrates a uniform volume doping throughout the WSe_2 surface and body, supporting the XAS results discussed earlier. Notably, the electrically extracted saturation doping concentration is consistent with that extracted from XPS measurements.

Contact resistance, R_c was extracted before and after NO_x chemisorption using the transfer line method (TLM).[24] Figure 6a shows the transfer characteristics of TLM devices with channel lengths of 500 nm, 1 μm, 1.5 μm, and 2 μm fabricated on a WSe_2 flake with a thickness of $\sim$7 nm (Figure 6b inset). The observed low I_{on} and ambipolar behavior prior to doping implies a large R_c due to Schottky barrier height near the WSe_2 midgap. After doping, however, we see a significant increase in I_{on} indicating a decrease in R_c. Using $R_{total} = 2R_{contact} + R_{channel}(L)$, where R_{total} and $R_{channel}$ are the unit-width normalized total resistance and channel resistance, R_c is found to be 0.13 GΩ/μm and 1.27

kΩ/μm before and after NO_x chemisorption, respectively (Figure 6b,c). NO_2 doping is shown to reduce the R_c by a remarkable 5 orders of magnitude. Finally, we revisit WSe_2 doping extraction including R_c, and find again consistent doping level $p \sim 1.6 \times 10^{19} cm^{-3}$.

CONCLUSION

In summary, we have demonstrated air stable p-doping of WSe_2 *via* covalent functionalization by NO_x at an elevated temperature of 150 °C. The stability of this covalent bonding scheme enables in-depth characterization *via* XAS and XPS, confirming $WSe_{2-x-y}O_xN_y$ species formation due to NO_x chemisorption on both the WSe_2 surface and body. From XPS, a shift of ~0.8 eV of E_F toward E_V also concludes a degenerate doping situation. In addition, all observed $WSe_{2-x-y}O_xN_y$ species are shown to be energetically favorable from *ab initio* simulations, with NO:WSe_2 identified as the dominant configuration leading to p-doping. Our time dependent doping study also indicates doping tunability, and the TLM study further confirms the extracted doping concentration of 1.6×10^{19} cm^{-3} while also showing a remarkable ~5 orders of magnitude R_c reduction *via* NO_x functionalization. Controllable semiconductor doping is an important and fundamental enabler in the general field of electronic devices, and degenerate materials can be utilized anywhere from contact materials to junctions in tunneling devices. Therefore, our demonstration of air stable doping through covalent functionalization of WSe_2 presents another route for further enhancing and manipulating TMDC functionalities and applications.

METHODS

Device Fabrication. The device fabrication starts with mechanical exfoliation of WSe_2 (Nanosurf) on top of a SiO_2 (260 nm)/Si substrate. Source/drain contacts are patterned using photolithography, and e-beam evaporation of Pd/Au (10/30 nm) films and resist liftoff in acetone.

NO_2 Doping. The fabricated sample is placed inside an evacuated 250 mL Pyrex glass flask with ambient N_2 flow for gas exchange. Subsequently, a constant NO_2 gas flow (5000 ppm balanced in N_2) is introduced through the flask and maintained throughout the entire doping procedure, exhausting to an external oil bath. Simultaneously, the flask is placed on a hot plate with the sample temperature maintained at 150 °C and doped for a set time. Finally, the sample is cooled first to ~50 °C before purging the flask with N_2 and sample removal.

XAS Characterizations. X-ray absorption spectroscopy of NO_x chemisorption in WSe_2 characterization was taken at Beamline 8.0.1 at Advanced Light Source, Lawrence Berkeley National Laboratory. N K-edge spectrum was calibrated carefully by measuring h-BN reference sample for energy calibration. The energy resolution at N K-edge region is about 0.1 eV and the vacuum of experiment chamber is lower than 5×10^{-9} Torr. All XAS spectra were recorded in Total Electron Yield (TEY) and Total Fluorescence Yield (TFY) simultaneously.

XPS Characterizations. The XPS spectra were acquired using a monochromated Al Kα source ($h\nu$ = 1486.7 eV) connected to a UHV cluster system described elsewhere.[25] An analyzer acceptance angle of ±8°, a take-off angle of 45°, and pass energy of 15 eV were used for this study. The binding energy scale is calibrated using the ASTM procedure.[26]

Optical, Electrical, Raman, PL, and XRD Characterizations. Optical images are taken with an Olympus BX51 microscope with an attached video camera. All electrical measurements are conducted on a HP 4155C analyzer with a corresponding probe station. Both Raman and PL are conducted using a commercially available HORIBA LabRAM HR800 system using an external laser source with an excitation wavelength of 532 nm. The X-ray diffraction (XRD) was taken on a Bruker AXS D8 Discover GADDS XRD Diffractometer system.

***Ab Initio* Simulations.** First-principles calculations were utilized based on DFT[27,28] with plane wave basis sets and Projector Augmented Wave (PAW) pseudopotentials[28,29] implemented in the Vienna *Ab initio* Simulation Package (VASP).[27,30,31] The electronic wave functions were represented by plane wave basis with a cutoff energy of 600 eV. The exchange and correlation interactions are incorporated as a functional of the Generalized Gradient Approximation (GGA).[29,32,33] A 5 × 5 supercell of monolayer WSe_2 host was used for the simulations. Each model has ~18 Å vacuum to avoid interaction between replica images as a result of the periodic boundary conditions. NO, NO_2 and O were separately placed near a singular Se vacancy of WSe_2 (or pristine WSe_2) and allowed to relax energetically while the host cell size was kept fixed after optimization.

Conflict of Interest: The authors declare no competing financial interest.

Supporting Information Available: Detailed device transfer characteristics after doping, and AFM of various flake thicknesses used. This material is available free of charge *via* the Internet at http://pubs.acs.org.

Acknowledgment. The device fabrication and characterization components of this work were supported by NSF E3S Center. The materials characterization and *ab initio* simulation were funded by the LEAST Center. The work at ALS is supported by the U.S. Department of Energy under the Contract No. DE-AC02-05CH11231. All the DFT calculations were performed using computational resources of Texas Advanced Computer Center (TACC) at University of Texas at Austin.

REFERENCES AND NOTES

1. Wang, Q. H.; Kalantar-Zadeh, K.; Kis, A.; Coleman, J. N.; Strano, M. S. Electronics and Optoelectronics of Two-Dimensional Transition Metal Dichalcogenides. *Nat. Nanotechnol.* **2012**, *7*, 699–712.
2. Jariwala, D.; Sangwan, V. K.; Lauhon, L. J.; Marks, T. J.; Hersam, M. C. Emerging Device Applications for Semiconducting Two-Dimensional Transition Metal Dichalcogenides. *ACS Nano* **2014**, *8*, 1102–1120.
3. Kiriya, D.; Tosun, M.; Zhao, P.; Kang, J. S.; Javey, A. Air-Stable Surface Charge Transfer Doping of MoS_2 by Benzyl Viologen. *J. Am. Chem. Soc.* **2014**, *136*, 7853–7856.
4. Fang, H.; Chuang, S.; Chang, T. C.; Takei, K.; Takahashi, T.; Javey, A. High-Performance Single Layered WSe2 p-FETs with Chemically Doped Contacts. *Nano Lett.* **2012**, *12*, 3788–3792.
5. Fang, H.; Tosun, M.; Seol, G.; Chang, T. C.; Takei, K.; Guo, J.; Javey, A. Degenerate n-Doping of Few-Layer Transition Metal Dichalcogenides by Potassium. *Nano Lett.* **2013**, *13*, 1991–1995.
6. Zhang, Y. L.; Wu, Z. F.; Chen, B. H.; Xu, L. S.; Pan, H. B.; Ma, Y. S.; Jiang, Z. Q.; Zhu, J. F.; Huang, W. X. Generating Oxygen Adatoms on Au(997) by Thermal Decomposition of NO_2. *Chin. Sci. Bull.* **2010**, *55*, 3889–3893.
7. Huffman, R. E.; Davidson, N. Shock Waves in Chemical Kinetics—The Thermal Decomposition of NO_2. *J. Am. Chem. Soc.* **1959**, *81*, 2311–2316.

8. Poteat, T. L.; Lalevic, B. Pd-MOS Hydrogen and Hydrocarbon Sensor Device. *IEEE Electron Device Lett.* **1981**, *2*, 82–84.
9. Liu, G.; Rodriguez, J. A.; Hrbek, J.; Dvorak, J.; Peden, C. H. F. Electronic and Chemical Properties of $Ce_{0.8}Zr_{0.2}O_2$(111) Surfaces: Photoemission, XANES, Density-Functional, and NO_2 Adsorption Studies. *J. Phys. Chem. B* **2001**, *105*, 7762–7770.
10. Okumura, K.; Amano, J.; Yasunobu, N.; Niwa, M. X-ray Absorption Fine Structure Study of the Formation of the Highly Dispersed PdO over ZSM-5 and the Structural Change of Pd Induced by Adsorption of NO. *J. Phys. Chem. B* **2000**, *104*, 1050–1057.
11. Overbury, S. H.; Mullins, D. R.; Huntley, D. R.; Kundakovic, L. Chemisorption and Reaction of NO and N_2O on Oxidized and Reduced Ceria Surfaces Studied by Soft X-Ray Photoemission Spectroscopy and Desorption Spectroscopy. *J. Catal.* **1999**, *186*, 296–309.
12. Tronc, M.; King, G. C.; Read, F. H. Nitrogen K-shell Excitation in N_2, NO and N_2O by High-Resolution Electron Energy-Loss Spectroscopy. *J. Phys. B: At., Mol. Opt. Phys.* **1980**, *13*, 999.
13. Wight, G. R.; Brion, C. E. K-shell Excitations in NO and O_2 by 2.5 keV electron impact. *J. Electron Spectrosc. Relat. Phenom.* **1974**, *4*, 313–325.
14. Colton, R. J.; Rabalais, J. W. Electronic Structure to Tungsten and Some of Its Borides, Carbides, Nitrides, and Oxides by X-ray Electron Spectroscopy. *Inorg. Chem.* **1976**, *15*, 236–238.
15. Biloen, P.; Pott, G. T. X-ray Photoelectron Spectroscopy Study of Supported Tungsten Oxide. *J. Catal.* **1973**, *30*, 169–174.
16. Kerkhof, F. P. J. M.; Moulijn, J. A.; Heeres, A. The XPS Spectra of the Metathesis Catalyst Tungsten Oxide on Silica Gel. *J. Electron Spectrosc. Relat. Phenom.* **1978**, *14*, 453–466.
17. Cho, D. H.; Chang, T. S.; Shin, C. H. Variations in the Surface Structure and Composition of Tungsten Oxynitride Catalyst Caused by Exposure to Air. *Catal. Lett.* **2000**, *67*, 163–169.
18. Joyce, W. B.; Dixon, R. W. Analytic Approximations for the Fermi Energy of an Ideal Fermi Gas. *Appl. Phys. Lett.* **1977**, *31*, 354–356.
19. Späh, R.; Lux-Steiner, M.; Obergfell, M.; Bucher, E.; Wagner, S. n-$MoSe_2$/p-WSe_2 Heterojunctions. *Appl. Phys. Lett.* **1985**, *47*, 871–873.
20. Zhao, W.; Ghorannevis, Z.; Amara, K. K.; Pang, J. R.; Toh, M.; Zhang, X.; Kloc, C.; Tan, P. H.; Eda, G. Lattice Dynamics in Mono- And Few-Layer Sheets of WS_2 and WSe_2. *Nanoscale* **2013**, *5*, 9677–9683.
21. Luo, X.; Zhao, Y.; Zhang, J.; Toh, M.; Kloc, C.; Xiong, Q.; Quek, S. Y. Effects of Lower Symmetry and Dimensionality on Raman Spectra in Two-Dimensional WSe_2. *Phys. Rev. B: Condens. Matter* **2013**, *88*, 195313.
22. Zhao, W.; Ghorannevis, Z.; Chu, L.; Toh, M.; Kloc, C.; Tan, P.-H.; Eda, G. Evolution of Electronic Structure in Atomically Thin Sheets of WS_2 and WSe_2. *ACS Nano* **2012**, *7*, 791–797.
23. Tonndorf, P.; Schmidt, R.; Böttger, P.; Zhang, X.; Börner, J.; Liebig, A.; Albrecht, M.; Kloc, C.; Gordan, O.; Zahn, D. R. T.; Michaelis de Vasconcellos, S.; Bratschitsch, R. Photoluminescence Emission and Raman Response of Monolayer MoS_2, $MoSe_2$, and WSe_2. *Opt. Express* **2013**, *21*, 4908–4916.
24. Berger, H. H. Models for Contacts to Planar Devices. *Solid-State Electron.* **1972**, *15*, 145–158.
25. Wallace, R. M. In-Situ Studies of Interfacial Bonding of High-k Dielectrics for CMOS beyond 22 nm. *ECS Trans.* **2008**, 255.
26. Standard Practice for Calibration of the Electron Binding-Energy Scale of an X-Ray Photoelectron Spectrometer. http://www.astm.org/Standards/E2108.htm (accessed August 14, 2014).
27. Kresse, G.; Furthmüller, J. Efficiency of *ab Initio* Total Energy Calculations for Metals and Semiconductors Using a Plane-Wave Basis Set. *Comput. Mater. Sci.* **1996**, *6*, 15–50.
28. Yang, R. G. P. a. W. *Density-Functional Theory of Atoms and Molecules*; Oxford University Press: New York, 1989.
29. Kohn, W.; Sham, L. J. Self-Consistent Equations Including Exchange and Correlation Effects. *Phys. Rev.* **1965**, *140*, A1133–A1138.
30. Blöchl, P. E. Projector Augmented-Wave Method. *Phys. Rev. B: Condens. Matter* **1994**, *50*, 17953–17979.
31. Kresse, G.; Joubert, D. From Ultrasoft Pseudopotentials to the Projector Augmented-Wave Method. *Phys. Rev. B: Condens. Matter* **1999**, *59*, 1758–1775.
32. Kresse, G.; Furthmüller, J. Efficient Iterative Schemes for *ab Initio* Total-Energy Calculations Using a Plane-Wave Basis Set. *Phys. Rev. B: Condens. Matter* **1996**, *54*, 11169–11186.
33. Kresse, G.; Hafner, J. *Ab Initio* Molecular Dynamics for Liquid Metals. *Phys. Rev. B: Condens. Matter* **1993**, *47*, 558–561.

Supporting Information

Air Stable *p*-Doping of WSe_2 by Covalent Functionalization

Peida Zhao[1,2], Daisuke Kiriya[1,2], Angelica Azcatl[3], Chenxi Zhang[3], Mahmut Tosun[1,2], Yi-Sheng Liu[4], Mark Hettick[1,2], Jeong Seuk Kang[1,2], Stephen McDonnell[3], Santosh KC[3], Jinghua Guo[4], Kyeongjae Cho[3], Robert M. Wallace[3], and Ali Javey[1,2,]*

[1] Electrical Engineering and Computer Sciences, University of California, Berkeley, CA 94720

[2] Materials Sciences Division, Lawrence Berkeley National Laboratory, Berkeley, CA 94720

[3] Materials Science and Engineering, The University of Texas at Dallas, Richardson, TX 95080

[4] Advanced Light Source, Lawrence Berkeley National Laboratory, Berkeley, CA 94720

[*]E-mail: ajavey@berkeley.edu

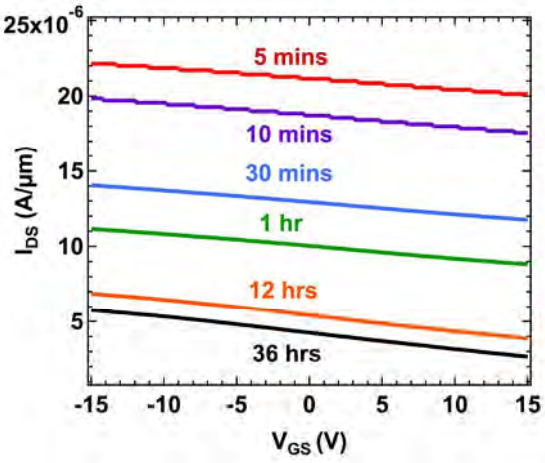

Figure S1. Facsimile of Figure 1(d) represented in linear scale for drain current. A degenerate p-type trend is observed with small on/off ratio and slightly lower drain current at a more positive gate bias.

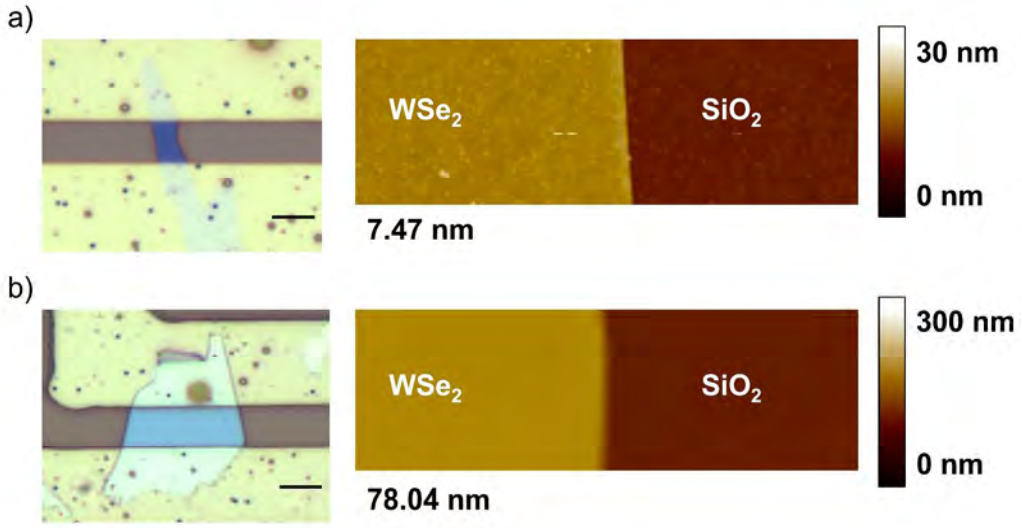

Figure S2. Optical microscopy (left) and atomic force microscopy (AFM, right) images of devices shown in Figure 5. WSe_2 layer thicknesses are (a) ~7.5nm and (b) ~ 78 nm. Scale bar is 3μm.